Chapter 3
Scattering Mechanisms

This chapter is devoted to the main mechanisms of scattering (elastic, quasi-elastic, and inelastic) that are relevant to the description of the interaction of electron beams with solid targets.

Firstly the elastic scattering cross-section will be described, comparing the screened Rutherford formula to the more accurate Mott cross-section [1]. The Mott theory is based on the relativistic partial wave expansion method and the numerical solution of the Dirac equation in a central field. The Mott cross-section is in better agreement with the available experimental data when electron energy is smaller than ∼5–10 keV.

We will also briefly describe the Fröhlich theory [2], which describes the quasi-elastic events occurring when electron energy is very low and the probability of electron–phonon interaction becomes significant. We will discuss energy loss and energy gain due to electron phonon-interactions, and see that electron energy gains can be safely neglected, while electron energy losses are fractions of eV.

The Bethe–Bloch stopping power formula [3] and semi-empiric approaches [4, 5] will be presented, along with the limits of these models for the calculation of energy losses.

The Ritchie dielectric theory [6] will then be considered, which is used for the accurate calculation of electron energy losses due to electron–plasmon interaction.

Polaronic effect will be also mentioned, as it is an important mechanism for trapping very slow electrons in insulating materials [7].

A discussion about the inelastic mean free path will be provided that takes into account all the inelastic scattering mechanisms introduced in this chapter.

Lastly, surface phenomena will be described along with numerical calculations of surface and bulk plasmon loss spectra.

Many details about the most important theoretical models presented in this chapter can be found in the Appendices.

M. Dapor, *Transport of Energetic Electrons in Solids*,
Springer Tracts in Modern Physics 257, DOI 10.1007/978-3-319-47492-2_3

3.1 Elastic Scattering

Electron-atom elastic scattering is the main responsible for the angle deflection of electrons traveling in solid targets. For some reviews about the subject of elastic scattering see, for example, Refs. [8–13].

Elastic scattering is not only the cause of the electron deflection: it also accounts for electron energy-loss problems, for it contributes to change the angular distribution of the inelastically scattered electrons [9, 10].

Since a nucleus is much more massive that an electron, the energy transfer is very small and, typically, negligible in an electron–nucleus collision. The great majority of elastic collisions regard the interaction of the incident electrons with the electrostatic nuclear field in regions that are far from the center of mass of the nucleus where, due to both the inverse square law and the shielding of the nucleus by the atomic electrons, the potential is relatively weak. For this reason, many electrons are elastically scattered through small angles.

Conservation of energy and momentum requires small transfers of energy between the electrons and the nuclei that depend on the angle of scattering. Even if the electron energy transfers are a very small fraction of eV, in many circumstances they cannot be neglected. Furthermore it has to be noted that, despite this general rule, in a few cases significant energy transfers are possible. Indeed, even if electron energy-losses are typically very small and often irrelevant in electron–nucleus collisions, for the very rare cases of head-on collisions, where the scattering angle is equal to 180°, the energy transfer can be, for the case of light elements, higher than the displacement energy, namely the energy necessary to displace the atom from its lattice position. In these cases, displacement damage and/or atom removal (sputtering) can be observed [9, 10, 14].

The differential elastic scattering cross-section represents the probability per unit solid angle that an electron be elastically scattered by an atom, and is given by the square modulus of the complex scattering amplitude f, which is a function of the scattering angle ϑ, of the incident electron energy E_0, and of the (mean) atomic number Z of the target. The angular distribution, once taken into account that the Coulomb potential is screened by the atomic electrons, can be calculated either by the use of the first Born approximation (screened Rutherford cross-section) or, in order to obtain more accurate results – in particular for low-energy electrons –, by solving the Schrödinger equation in a central field (partial wave expansion method, PWEM).

Typically, for the case of the screened Rutherford formula obtained within the first Born approximation, the screening of atomic electrons is described by the Wentzel formula [15], which corresponds to a Yukawa exponential attenuation of the nuclear potential as a function of the distance from the center of mass of the nucleus. The more accurate partial wave expansion method requires a better description of the screening, so that Dirac–Hartree–Fock–Slater methods are generally used for calculating the screened nuclear potential in this case.

A further improved approach for obtaining a very accurate calculation of the differential elastic scattering cross-section, valid also for relativistic electrons, is the so-called relativistic partial wave expansion method (RPWEM), – which is based on the solution of the Dirac equation in a central field (Mott cross-section) – where the sum of the squares of the moduli of two complex scattering amplitudes f and g is required for the calculation of the elastic scattering probabilities [1]. Also in this case, Dirac–Hartree–Fock–Slater methods are utilized to calculate the shielded nuclear potential.

3.1.1 Mott Cross-Section Versus Screened Rutherford Cross-Section

The relativistic partial wave expansion method (Mott theory) [1] permits to calculate the differential elastic scattering cross-section as follows:

$$\frac{d\sigma_{\mathrm{el}}}{d\Omega} = \mid f \mid^2 + \mid g \mid^2 , \tag{3.1}$$

where $f(\vartheta)$ and $g(\vartheta)$ are the scattering amplitudes (direct and spin-flip, respectively). For details about the Mott theory and the calculation of the scattering amplitudes $f(\vartheta)$ and $g(\vartheta)$, see Chap. 11 and Refs. [11, 13]. Also see Refs. [12, 16–18] for several applications.

Once the differential elastic scattering cross-section has been calculated, the total elastic scattering cross-section σ_{el} and the first transport elastic scattering cross-section σ_{tr} can be computed using the following equations:

$$\sigma_{\mathrm{el}} = \int \frac{d\sigma_{\mathrm{el}}}{d\Omega}\, d\Omega , \tag{3.2}$$

$$\sigma_{\mathrm{tr}} = \int (1 - \cos\vartheta)\, \frac{d\sigma_{\mathrm{el}}}{d\Omega}\, d\Omega . \tag{3.3}$$

It can be interesting to investigate the high energy and low atomic number limits of the Mott theory (corresponding to the first Born approximation). Along with the assumption that the atomic potential can be written according to the Wentzel formula [15]:

$$V(r) = -\frac{Z\, e^2}{r} \exp\left(-\frac{r}{a}\right) , \tag{3.4}$$

where r is the distance between the incident electron and the nucleus, Z the target atomic number, e the electron charge, and a approximately represents the screening of the nucleus by the orbital electrons, given by

$$a = \frac{a_0}{Z^{1/3}}, \tag{3.5}$$

where a_0 is the Bohr radius, the first Born approximation permits to write the differential elastic scattering cross-section in an analytic closed form. It is the so-called screened Rutherford cross-section:

$$\frac{d\sigma_{\mathrm{el}}}{d\Omega} = \frac{Z^2 e^4}{4E^2} \frac{1}{(1 - \cos\theta + \alpha)^2}, \tag{3.6}$$

$$\alpha = \frac{me^4\pi^2}{h^2} \frac{Z^{2/3}}{E} \tag{3.7}$$

In these equations, m is the electron mass and h is the Planck constant.

The screened Rutherford formula has been largely used even if it is unable to describe all the features corresponding to the elastic scattering as a function of the scattering angle that one can observe when incident electron kinetic energies are lower than ~5–10 keV and the target atomic number is relatively high. In Figs. 3.1, 3.2, 3.3 and 3.4 the differential elastic scattering cross-section $d\sigma_{\mathrm{el}}/d\Omega$ (DESCS) – calculated with both the Mott and the Rutherford theories – are compared. The presented data concern two different elements (Cu and Au) and two different energies (1000 and 3000 eV). From the comparison clearly emerges that the Rutherford theory approaches the Mott theory as the atomic number decreases and the primary energy increases. Indeed, the Rutherford formula can be deduced assuming the first Born approximation, which is valid when

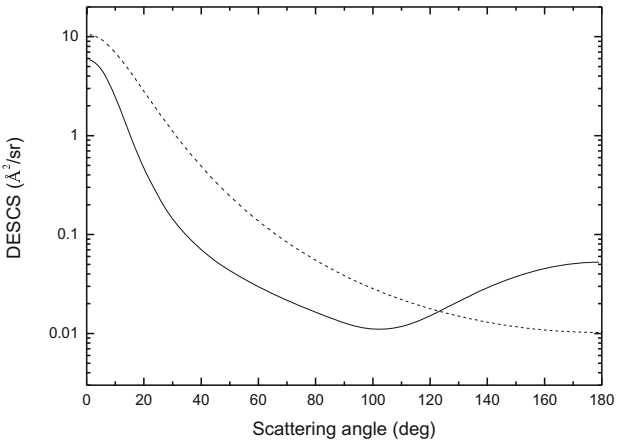

Fig. 3.1 Calculation of the differential elastic scattering cross-section of 1000 eV electrons scattered by Cu as a function of the scattering angle. *Solid line* Relativistic partial wave expansion method (Mott theory). *Dashed line* Screened Rutherford formula, Eq. (3.6)

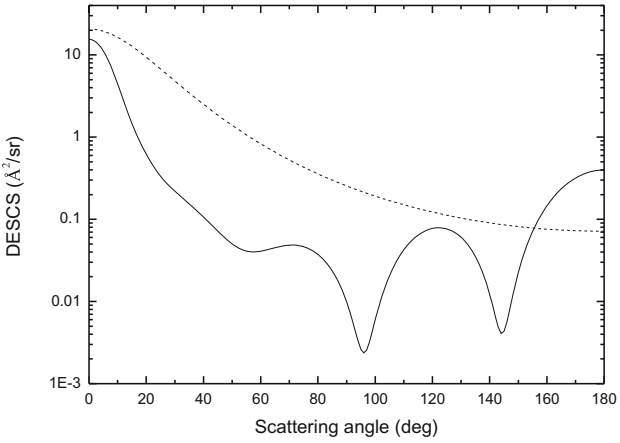

Fig. 3.2 Calculation of the differential elastic scattering cross-section of 1000 eV electrons scattered by Au as a function of the scattering angle. *Solid line* Relativistic partial wave expansion method (Mott theory). *Dashed line* Screened Rutherford formula, Eq. (3.6)

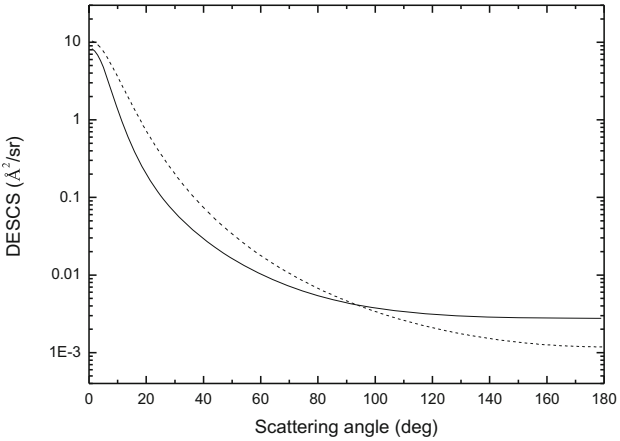

Fig. 3.3 Calculation of the differential elastic scattering cross-section of 3000 eV electrons scattered by Cu as a function of the scattering angle. *Solid line* Relativistic partial wave expansion method (Mott theory). *Dashed line* Screened Rutherford formula, Eq. (3.6)

$$E \gg \frac{e^2}{2a_0} Z^2 \,. \tag{3.8}$$

In other words, the higher the electron energy – in comparison with the atomic potential – the higher the accuracy of the Rutherford theory (see, in particular, Fig. 3.3). Anyway, the Rutherford formula represents a decreasing function of the scattering angle, so that it should not be surprising that it cannot describe the features that emerge as the electron energy is low and the atomic number is high (see, in particular, Fig. 3.2).

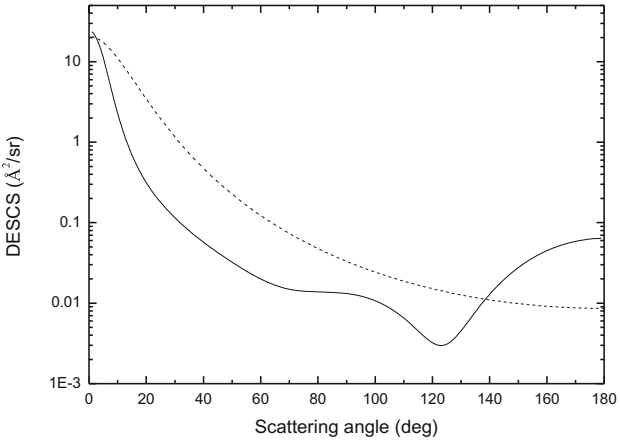

Fig. 3.4 Calculation of the differential elastic scattering cross-section of 3000 eV electrons scattered by Au as a function of the scattering angle. *Solid line* Relativistic partial wave expansion method (Mott theory). *Dashed line* Screened Rutherford formula, Eq. (3.6)

In Monte Carlo simulations, when the electron primary energy is higher than 10 keV, Rutherford cross-section is sometimes used – instead of the more accurate Mott cross-section – mainly because it provides a very simple analytic way to calculate both the cumulative probability of elastic scattering into an angular range from 0 to θ, $P_{\rm el}(\theta, E)$, and the elastic scattering mean free path, $\lambda_{\rm el}$. Even if not used by the simulations presented in this book, where numerical calculations of Mott cross-section will always be utilized (see Fig. 3.5, where Mott cross section is represented for 1000 eV electrons in Al), it might be useful to see how $P_{\rm el}(\theta, E)$ and $\lambda_{\rm el}$ can be calculated in a completely analytic way taking advantage of the particular form of the screened Rutherford formula. In the first Born approximation these quantities are in fact given, respectively, by

$$P_{\rm el}(\theta, E) = \frac{(1 + \alpha/2)\,(1 - \cos\theta)}{1 + \alpha - \cos\theta}\,, \tag{3.9}$$

$$\lambda_{\rm el} = \frac{\alpha\,(2 + \alpha)\,E^2}{N\,\pi\,e^4\,Z^2}\,, \tag{3.10}$$

where N is the number of atoms per unit volume in the target. The demonstration of these equations is quite easy. Indeed

$$P_{\rm el}(\theta, E) = \\ = \frac{e^4 Z^2}{4\sigma_{\rm el} E^2} \int_0^{\theta} \frac{2\pi \sin\vartheta\, d\vartheta}{(1 - \cos\vartheta + \alpha)^2} = \frac{\pi e^4 Z^2}{2\sigma_{\rm el} E^2} \int_{\alpha}^{1-\cos\theta+\alpha} \frac{du}{u^2}\,,$$

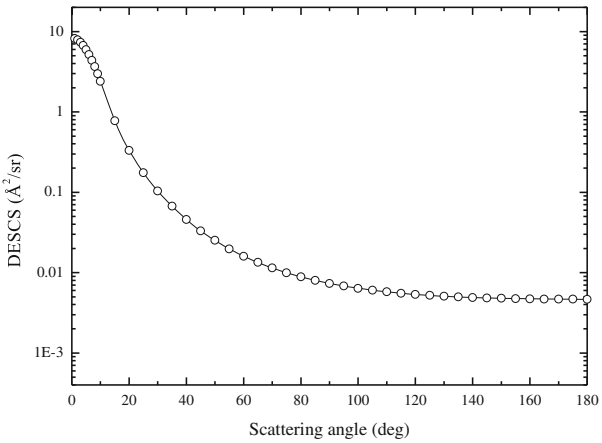

Fig. 3.5 Differential elastic scattering cross-section of 1000 eV electrons scattered by Al as a function of the scattering angle. *Solid line* Present calculations (Mott theory) [13]. *Circles* Salvat and Mayol calculations (Mott theory) [19]

where

$$\sigma_{\mathrm{el}} = \frac{e^4 Z^2}{4E^2} \int_0^{\pi} \frac{2\pi \sin\vartheta \, d\vartheta}{(1 - \cos\vartheta + \alpha)^2} = \frac{\pi e^4 Z^2}{2E^2} \int_{\alpha}^{2+\alpha} \frac{du}{u^2} .$$

Since

$$\int_{\alpha}^{1-\cos\theta+\alpha} \frac{du}{u^2} = \frac{1 - \cos\theta}{\alpha(1 - \cos\theta + \alpha)}$$

and

$$\int_{\alpha}^{2+\alpha} \frac{du}{u^2} = \frac{1}{\alpha(1 + \alpha/2)} ,$$

Equations (3.9) and (3.10) immediately follow.

Note that from the cumulative probability expressed by Eq. (3.9) it follows that the scattering angle can be easily calculated from:

$$\cos\theta = 1 - \frac{2\alpha \, P_{\mathrm{el}}(\theta, E)}{2 + \alpha - 2P_{\mathrm{el}}(\theta, E)} . \tag{3.11}$$

Due to the excellent agreement between experimental data and Mott cross-section (see, for a comparison, Fig, 3.6), the most recent Monte Carlo codes (and also all

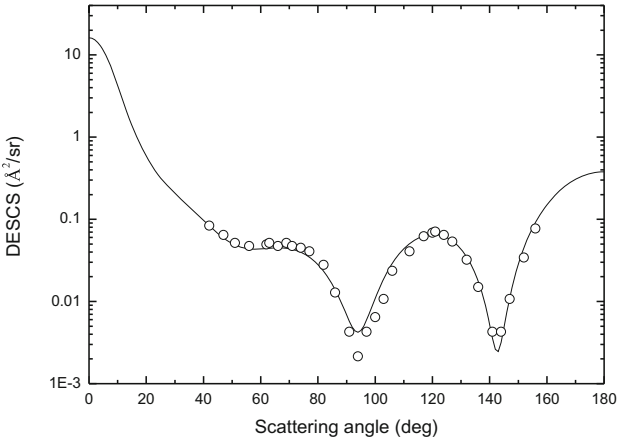

Fig. 3.6 Differential elastic scattering cross-section of 1100 eV electrons scattered by Au as a function of the scattering angle. *Solid line* Present calculations (Mott theory) [13]. *Circles* Reichert experimental data [20]

the calculations presented in this book) use the Mott cross-section to describe the differential elastic scattering cross-section – and the cumulative probability necessary for sampling the scattering angle. Nevertheless, it is worth stressing that excellent results can also be obtained using the simple screened Rutherford formula, Eq. (3.6), provided that the kinetic primary energy of the incident electrons is higher than 10 keV [21].

3.2 Quasi-elastic Scattering

Due to thermal excitations, atoms in crystalline structures vibrate around their equilibrium lattice sites. These vibrations are known as *phonons*. A mechanism of energy loss (and energy gain as well) is represented by the interaction of the electrons with the optical modes of the lattice vibrations. These transfers of small amounts of energy among electrons and lattice vibrations are due to quasi-elastic processes known as *phonon creation* (electron energy-loss) and *phonon annihilation* (electron energy-gain) [2, 22]. Phonon energies do not exceed $k_B T_D$, where k_B is the Boltzmann constant and T_D is the Debye temperature. As typically $k_B T_D$ is not greater than 0.1 eV, the energy losses and gains due to electron–phonon interaction are usually smaller than 0.1 eV, so that they are generally not resolved by conventional spectrometers [9]. These mechanisms of electron energy loss – and, with much smaller probability, energy gain – are particularly relevant when the electron energy is low (few eV) [7].

3.2.1 Electron–Phonon Interaction

According to Fröhlich [2] and Llacer and Garwin [22], the inverse mean free path for electron energy loss due to phonon creation can be written as

$$\lambda_{\text{phonon}}^{-1} = \frac{1}{a_0} \frac{\varepsilon_0 - \varepsilon_\infty}{\varepsilon_0\, \varepsilon_\infty} \frac{\hbar\omega}{E} \frac{n(T) + 1}{2} \ln\left[\frac{1 + \sqrt{1 - \hbar\omega/E}}{1 - \sqrt{1 - \hbar\omega/E}}\right], \tag{3.12}$$

where E is the energy of the incident electron, $W_{\text{ph}} = \hbar\omega$ the electron energy loss (in the order of 0.1 eV), ε_0 the static dielectric constant, ε_∞ the high frequency dielectric constant, a_0 the Bohr radius and

$$n(T) = \frac{1}{e^{\hbar\omega/k_{\text{B}}T} - 1} \tag{3.13}$$

the occupation number. Notice that a similar equation can be written to describe electron energy gain (corresponding to phonon annihilation). The occurrence probability of phonon annihilation is much lower than that of phonon creation. Electron energy gain can thus be safely neglected for many practical purposes.

For further details about electron–phonon interaction and Fröhlich theory [2, 22] see Chap. 12.

3.3 Inelastic Scattering

Let us consider now the inelastic scattering due to the interaction of the incident electrons with the atomic electrons located around the nucleus (both the core and the valence electrons). For an excellent review about this subject, see Ref. [9].

If the incident electron energy is high enough, it can excite an *inner-shell* electron that can make a transition from its ground state to one of the unoccupied electron states above the Fermi level. Due to energy conservation, the incident electron loses an amount of energy equal to the difference between the state above the Fermi level occupied by the excited atomic electron and its ground state; while the atom is left in an ionized state. The following de-excitation of the target atom generates an excess energy that can be released in one of two competitive ways: either generating an X-ray photon (Energy dispersive spectroscopy, EDS, is based on this process) or by the emission of another electron: this is the phenomenon on which Auger electron spectroscopy, AES, is based.

Outer-shell inelastic scattering can occur according to two alternative processes. In the first one, an outer-shell electron can suffer a single-electron excitation. A typical example is constituted by inter-band and intra-band transitions. If the atomic electron excited in such a way is able to reach the surface with an energy higher than the potential barrier between the vacuum level and the minimum of the conduction band,

it can emerge from the solid as a secondary electron, the energy needed for this transition being provided by the fast incident electron. De-excitation can occur through the emission of electromagnetic radiation in the visible region – corresponding to the phenomenon known as cathode-luminescence – or through radiation-less processes generating heat. Outer-shell electrons can also be excited in collective states corresponding to the oscillation of the valence electrons denoted as plasma resonance. It is generally described as the creation of quasi-particles known as *plasmons*, with energies – characteristic of the material – that range, typically, in the interval from 5 to 30 eV. Plasmon decay generates secondary electrons and/or produces heat.

3.3.1 Stopping: Bethe–Bloch Formula

In the continuous-slowing-down approximation, energy losses are calculated by utilizing the stopping power. Using a quantum mechanical treatment, Bethe [3] proposed the following formula for the stopping power:

$$-\frac{dE}{dz} = \frac{2\pi e^4 N Z}{E} \ln\left(\frac{1.166E}{I}\right), \tag{3.14}$$

where I represents the mean ionization energy which, according to Berger and Seltzer [23], can be approximated by the following simple formula:

$$I = (9.76 + 58.8\, Z^{-1.19})\, Z\,. \tag{3.15}$$

The Bethe–Bloch formula is valid for energies higher than $\sim I$. It approaches zero as E approaches $I/1.166$. When E becomes smaller than $I/1.166$, the stopping power predicted by the Bethe–Bloch formula becomes negative. Therefore, the low-energy stopping power requires a different approach (see the dielectric approach below).

3.3.2 Stopping: Semi-empiric Formulas

The stopping power can also be described using semi-empiric expressions, such as the following;

$$-\frac{dE}{dz} = \frac{K_e N Z^{8/9}}{E^{2/3}}, \tag{3.16}$$

proposed in 1972 by Kanaya and Okayama (with $K_e = 360\,\text{eV}^{5/3}\,\text{Å}^2$) [5]. The latter formula allows to analytically evaluate the maximum range of penetration R as a function of the primary energy E_0, where

$$R = \int_{E_0}^{0} \frac{dE}{dE/dz} = \frac{3E_0^{5/3}}{5K_e N Z^{8/9}} \propto E_0^{1.67}. \tag{3.17}$$

A similar empirical formula for the evaluation of the maximum range of penetration of electrons in solid targets was proposed, for the first time in 1954, by Lane and Zaffarano [4] who found that their range-energy experimental data (obtained by investigating electron transmission in the energy range 0–40 keV by thin plastic and metal films) fell within 15 % of the results obtained by the following simple equation:

$$E_0 = 22.2 R^{0.6}, \tag{3.18}$$

where E_0 was expressed in keV and R in mg/cm^2. As a consequence, the Kanaya and Okayama formula is consistent with the Lane and Zaffarano experimental observations, which are described as well by the relationship

$$R \propto E_0^{1.67}. \tag{3.19}$$

3.3.3 Dielectric Theory

In order to obtain a very accurate description of the electron energy loss processes, of the stopping power, and of the inelastic mean free path, valid even when electron energy is low, it is necessary to consider the response of the ensemble of conduction electrons to the electromagnetic field generated by the electrons passing through the solid: this response is described by a complex dielectric function. In Chap. 13 the Ritchie theory [6, 24] is described: it demonstrates, in particular, that the energy loss function, $f(k, \omega)$, necessary to calculate both the stopping power and the inelastic mean free path, is the reciprocal of the imaginary part of the dielectric function

$$f(k, \omega) = \mathrm{Im}\left[\frac{1}{\varepsilon(k, \omega)}\right]. \tag{3.20}$$

In Eq. (3.20), $\hbar\mathbf{k}$ represents the momentum transferred and $\hbar\omega$ the electron energy loss.

Once the energy loss function has been obtained, the differential inverse inelastic mean free path can be calculated as [25]

$$\frac{d\lambda_{\mathrm{inel}}^{-1}}{d\hbar\omega} = \frac{1}{\pi E a_0} \int_{k_-}^{k_+} \frac{dk}{k} f(k, \omega), \tag{3.21}$$

where

$$\hbar k_{\pm} = \sqrt{2mE} \pm \sqrt{2m(E - \hbar\omega)}, \tag{3.22}$$

E is the electron energy, m the electron mass, and a_0 the Bohr radius. The limits of integration, expressed by Eq. (3.22), come from conservation laws (see Sect. 5.2.3).

In order to calculate the dielectric function, and hence the energy loss-function, let us consider the electric displacement $\boldsymbol{\mathcal{D}}$ [17, 18]. If $\boldsymbol{\mathcal{P}}$ is the polarization density of the material, and $\boldsymbol{\mathcal{E}}$ the electric field, then

$$\boldsymbol{\mathcal{P}} = \chi_\varepsilon \boldsymbol{\mathcal{E}}\,, \tag{3.23}$$

where

$$\chi_\varepsilon = \frac{\varepsilon - 1}{4\pi} \tag{3.24}$$

and

$$\boldsymbol{\mathcal{D}} = \boldsymbol{\mathcal{E}} + 4\pi\boldsymbol{\mathcal{P}} = (1 + 4\pi\chi_\varepsilon)\boldsymbol{\mathcal{E}} = \varepsilon\boldsymbol{\mathcal{E}}\,. \tag{3.25}$$

If n is the density of the outer-shell electrons, i.e., the number of outer-shell electrons per unit volume in the solid, and ξ the electron displacement due to the electric field, then

$$\boldsymbol{\mathcal{P}} = e\,n\,\xi\,, \tag{3.26}$$

so that

$$|\boldsymbol{\mathcal{E}}| = \frac{4\pi e\,n\,\xi}{\varepsilon - 1}\,. \tag{3.27}$$

Let us consider the classical model of electrons elastically bound, with elastic constants $k_\mathrm{n} = m\omega_\mathrm{n}^2$ and subject to a frictional damping effect, due to collisions, described by a damping constant Γ. We have indicated here with m the electron mass and with ω_n the natural frequencies. The electron displacement satisfies the equation [26]

$$m\,\ddot{\xi} + \beta\dot{\xi} + k_\mathrm{n}\,\xi = e\,\boldsymbol{\mathcal{E}} \tag{3.28}$$

where $\beta = m\Gamma$. Assuming that $\xi = \xi_0 \exp(i\omega t)$, a straightforward calculation allows to conclude that

$$\varepsilon(0,\omega) = 1 - \frac{\omega_\mathrm{p}^2}{\omega^2 - \omega_\mathrm{n}^2 - i\,\Gamma\omega}\,, \tag{3.29}$$

where ω_p is the *plasma frequency*, given by

$$\omega_\mathrm{p}^2 = \frac{4\pi n\,e^2}{m}\,. \tag{3.30}$$

Let us now consider a superimposition of free and bound oscillators. In such a case the dielectric function can be written as:

$$\varepsilon(0,\omega) = 1 - \omega_{\mathrm{p}}^2 \sum_n \frac{f_{\mathrm{n}}}{\omega^2 - \omega_{\mathrm{n}}^2 - i\,\Gamma_{\mathrm{n}}\omega}\,, \tag{3.31}$$

where Γ_{n} are positive frictional damping coefficients and f_{n} are the fractions of the valence electrons bound with energies $\hbar\omega_{\mathrm{n}}$.

The extension of the dielectric function from the optical limit (corresponding to $k = 0$) to $k > 0$ is obtained including, in the previous formula, an energy $\hbar\omega_k$ related to the dispersion relation, so that

$$\varepsilon(k,\omega) = 1 - \omega_p^2 \sum_n \frac{f_n}{\omega^2 - \omega_n^2 - \omega_k^2 - i\,\Gamma_n\omega}\,. \tag{3.32}$$

In the determination of the dispersion relation, one has to take into account a constraint, known as the *Bethe ridge*. According to the Bethe ridge, as $k \to \infty$, $\hbar\omega_k$ should approach $\hbar^2k^2/2m$. Of course, an obvious way to obtain this result (the simplest one, actually) is to assume that [25, 27],

$$\hbar\omega_k = \frac{\hbar^2k^2}{2m}\,. \tag{3.33}$$

Another way of satisfying the constraint represented by the Bethe ridge is to use, according to Ritchie [6] and to Richie and Howie [24], the following equation :

$$\hbar^2\,\omega_k^2 = \frac{3\,\hbar^2\,v_F^2\,k^2}{5} + \frac{\hbar^4\,k^4}{4\,m^2}\,, \tag{3.34}$$

where v_F represents the velocity of Fermi.

Once the dielectric function is known, the loss function $\mathrm{Im}[1/\varepsilon(k,\omega)]$ is given by

$$\mathrm{Im}\left[\frac{1}{\varepsilon(k,\omega)}\right] = -\frac{\varepsilon_2}{\varepsilon_1^2 + \varepsilon_2^2}\,, \tag{3.35}$$

where

$$\varepsilon(k,\omega) = \varepsilon_1(k,\omega) + i\varepsilon_2(k,\omega)\,, \tag{3.36}$$

The calculation of the energy loss function can be also performed through the direct use of experimental optical data. In Figs. 3.7 and 3.8, the optical energy loss function of polymethyl methacrylate and silicon dioxide are represented, respectively.

A quadratic extension into the energy- and momentum-transfer plane of the energy loss function allows the extension of the dielectric function from the optical limit to $k > 0$ [32–34].

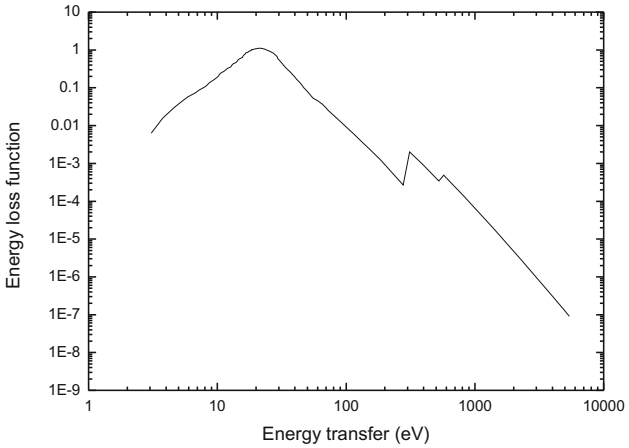

Fig. 3.7 Optical energy loss function for electrons in Polymethyl Methacrylate. For energies lower than 72 eV we used the optical data of Ritsko et al. [28]. For higher energies the calculation of the optical loss function was performed by using the Henke et al. atomic photo-absorption data [29, 30]

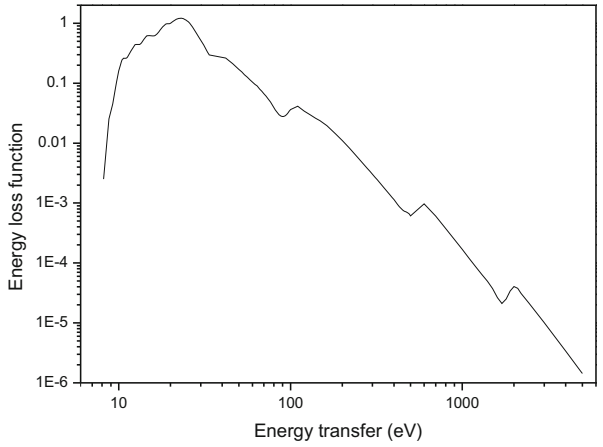

Fig. 3.8 Optical energy loss function for electrons in silicon dioxide (SiO_2). For energies lower than 33.6 eV we used the optical data of Buechner [31]. For higher energies the calculation of the optical loss function was performed by using the Henke et al. atomic photo-absorption data [29, 30]

Penn [32] and Ashley [33, 34] calculated the energy loss function by using optical data and by extending as discussed above the dielectric function from the optical limit to $k > 0$. According to Ashley [33, 34], the inverse inelastic mean free path $\lambda_{\text{inel}}^{-1}$ of electrons penetrating solid targets can be calculated by:

$$\lambda_{\text{inel}}^{-1}(E) = \frac{me^2}{2\pi\hbar^2 E} \int_0^{W_{max}} \text{Im}\left[\frac{1}{\varepsilon(0, w)}\right] L\left(\frac{w}{E}\right) dw\,, \tag{3.37}$$

where E is the incident electron energy and $W_{\max} = E/2$ (as usual, we have indicated with e the electron charge and with $\hbar$ the Planck constant h divided by 2π). According to Ashley, in the dielectric function $\varepsilon(\boldsymbol{k}, w)$, the momentum transfer $\hbar\boldsymbol{k}$ was set to 0 and the ε dependence on $\boldsymbol{k}$ was factorised through the function $L(w/E)$. Ashley [33] demonstrated that a good approximation of the function $L(x)$ is given by:

$$L(x) = (1-x)\ln\frac{4}{x} - \frac{7}{4}x + x^{3/2} - \frac{33}{32}x^2 . \tag{3.38}$$

The calculation of the stopping power, $-dE/dz$, can be performed by using the following equation [33]:

$$-\frac{dE}{dz} = \frac{me^2}{\pi\hbar^2 E}\int_0^{W_{\max}} \mathrm{Im}\left[\frac{1}{\varepsilon(0,w)}\right] S\left(\frac{w}{E}\right) w\, dw , \tag{3.39}$$

where

$$S(x) = \ln\frac{1.166}{x} - \frac{3}{4}x - \frac{x}{4}\ln\frac{4}{x} + \frac{1}{2}x^{3/2} - \frac{x^2}{16}\ln\frac{4}{x} - \frac{31}{48}x^2 . \tag{3.40}$$

The inelastic mean free path and the stopping power for positrons may be calculated in a similar way [34]:

$$(\lambda_{\mathrm{inel}}^{-1})_{\mathrm{p}} = \frac{me^2}{2\pi\hbar^2 E}\int_0^{W_{\max}} \mathrm{Im}\left[\frac{1}{\varepsilon(0,w)}\right] L_{\mathrm{p}}\left(\frac{w}{E}\right) dw , \tag{3.41}$$

$$\left(-\frac{dE}{dz}\right)_{\mathrm{p}} = \frac{me^2}{2\pi\hbar^2 E}\int_0^{W_{\max}} \mathrm{Im}\left[\frac{1}{\varepsilon(0,w)}\right] S_{\mathrm{p}}\left(\frac{w}{E}\right) w\, dw , \tag{3.42}$$

where

$$L_{\mathrm{p}}(x) = \ln\left(\frac{1 - x/2 + \sqrt{1-2x}}{1 - x/2 - \sqrt{1-2x}}\right) \tag{3.43}$$

and

$$S_{\mathrm{p}}(x) = \ln\left(\frac{1 - x + \sqrt{1-2x}}{1 - x - \sqrt{1-2x}}\right) . \tag{3.44}$$

In Figs. 3.9 and 3.10 the stopping powers of electrons in PMMA and in SiO_2 are, respectively, shown. In Figs. 3.11 and 3.12 the inelastic mean free paths of electrons in PMMA and in SiO_2 are also, respectively, represented. The present calculations, obtained using the Ashley theory that we just described. are compared with results of other authors.

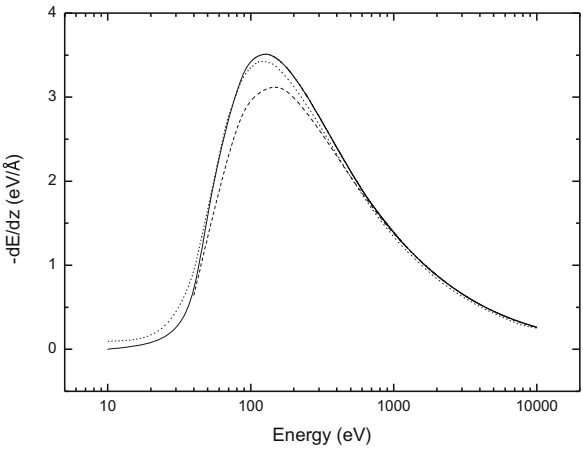

Fig. 3.9 Stopping power of electrons in PMMA. The *solid line* represents the present calculation, obtained according to the Ashley recipe [33]. The *dashed line* provides the Ashley original results [33]. *Dotted line* describes the Tan et al. computational results [35]. The different optical energy loss functions used in the three cases explain the differences in the calculations

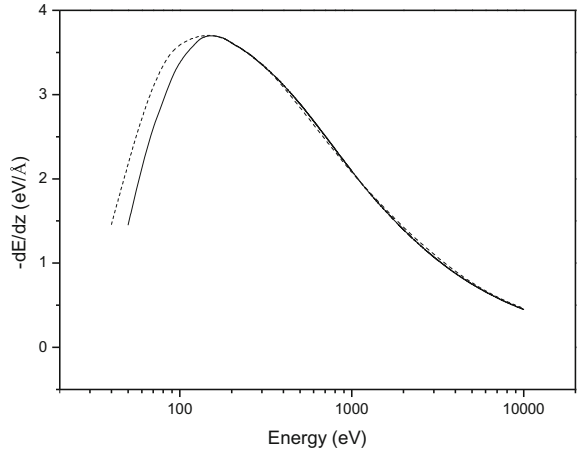

Fig. 3.10 Stopping power of electrons in SiO_2. The *solid line* represents the present calculation, obtained according to the Ashley recipe [33]. The *dashed line* provides the Ashley and Anderson data [36]. The different optical energy loss functions utilized in the two cases explain the differences in the calculations

Once $\varepsilon(0, w)$ is known, the electron differential inverse inelastic mean free path $d\lambda_{\text{inel}}^{-1}(w, E)/dw$ can be calculated by using the following equation:

$$\frac{d\lambda_{\text{inel}}^{-1}(w, E)}{dw} = \frac{me^2}{2\pi\hbar^2 E}\text{Im}\left[\frac{1}{\varepsilon(0, w)}\right] L\left(\frac{w}{E}\right) . \tag{3.45}$$

3.3.4 Sum of Drude Functions

Ritchie and Howie [24] have proposed to calculate the energy loss function as a linear superimposition of Drude functions, as follows:

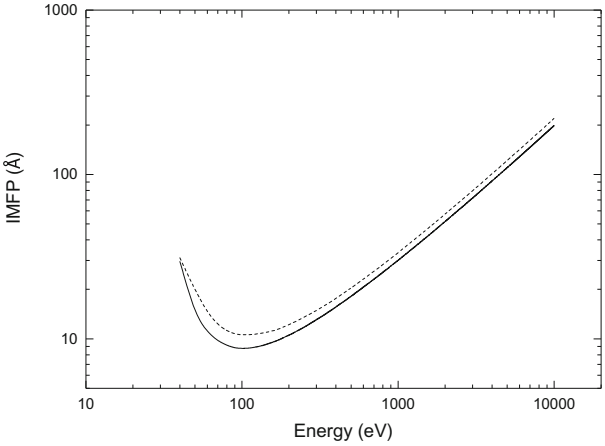

Fig. 3.11 Inelastic mean free path of electrons in PMMA due to electron–electron interaction. The *solid line* represents the present calculation, based on the Ashely model [33]. The *dashed line* describes the original Ashley results [33]. The differences in the two calculations are due to the different optical energy loss functions utilized

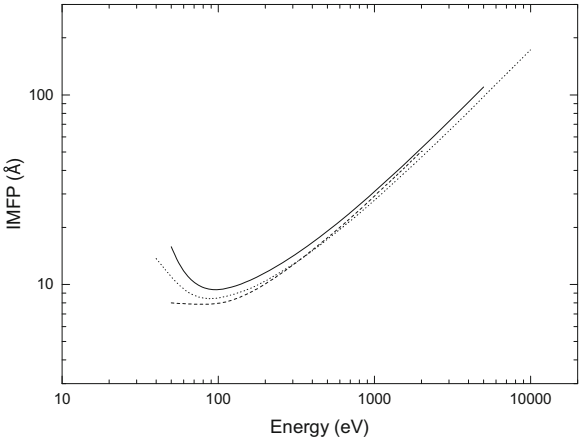

Fig. 3.12 Inelastic mean free path of electrons in SiO_2 due to electron–electron interaction. The *solid line* represents the present calculation, based on the Ashely model [33]. The *dashed line* describes the Ashley and Anderson data [36]. The *dotted line* provides the Tanuma, Powell and Penn computational results [37]. The differences in the calculations are due to the different optical energy loss functions utilized

$$\mathrm{Im}\left[\frac{1}{\varepsilon(k,\omega)}\right] = \sum_{\mathrm{n}} \frac{A_{\mathrm{n}}\,\Gamma_{\mathrm{n}}\,\hbar\omega}{[w_{\mathrm{n}}^2(k) - \hbar^2\omega^2]^2 + \hbar^2\omega^2\Gamma_{\mathrm{n}}^2}\,, \tag{3.46}$$

where, according to Eq. (3.34),

$$w_{\mathrm{n}}(k) = \sqrt{w_{\mathrm{n}}^2 + \frac{12E_{\mathrm{F}}}{5}\frac{\hbar^2k^2}{2m} + \left(\frac{\hbar^2k^2}{2m}\right)^2}\,, \tag{3.47}$$

Table 3.1 Parameters calculated by Garcia-Molina et al. [39] to fit the contribution to the optical energy loss function of the outer electrons for five selected carbon allotropes (amorphous carbon, glassy carbon, C60-fullerite, graphite, and diamond)

Target	n	w_n (eV)	Γ_n (eV)	A_n (eV^2)
Amorphous carbon	1	6.26	5.71	9.25
	2	25.71	13.33	468.65
Glassy carbon	1	2.31	4.22	0.96
	2	5.99	2.99	6.31
	3	19.86	6.45	77.70
	4	23.67	12.38	221.87
	5	38.09	54.42	110.99
C60-fullerite	1	6.45	2.45	6.37
	2	14.97	6.26	16.52
	3	24.49	13.06	175.13
	4	28.57	12.24	141.21
	5	40.82	27.21	141.47
Graphite	1	2.58	1.36	0.18
	2	6.99	1.77	7.38
	3	21.77	8.16	73.93
	4	28.03	6.80	466.69
	5	38.09	68.03	103.30
Diamond	1	22.86	2.72	22.21
	2	29.93	13.61	140.64
	3	34.77	11.43	843.85

In these equations, E_F is the Fermi energy, and w_n, Γ_n, A_n are the excitation energies, the damping constants, and the strengths, for $k = 0$ [38]. Garcia-Molina et al. [39] provided, for example, the values of these parameters, calculated from the fit of experimental optical data for five allotropic forms of carbon (amorphous carbon, glassy carbon, C60-fullerite, graphite, and diamond). In Table 3.1 the Garcia-Molina et al. parameters have been reported, for the reader's convenience. The optical energy loss functions so calculated for these five carbon allotrops are represented in Fig. 3.13.

In Fig. 3.14 the differential inverse inelastic mean free path for the considered allotrops of carbon, calculated by [see Eqs. (3.20) and (3.21)]

$$\frac{d\lambda_{\text{inel}}^{-1}}{d\hbar\omega} = \frac{1}{\pi a_0 E}\int_{k_-}^{k_+}\frac{dk}{k}\,\text{Im}\left[\frac{1}{\varepsilon(k,\omega)}\right], \tag{3.48}$$

where k_- and k_+ are given by Eq. (3.22), is represented as a function of the energy loss $w = \hbar\omega$ for incident electron energy $E = 250\,\text{eV}$. The comparison with the shapes of the curves representing the optical energy loss function of Fig. 3.13 clearly shows the effect of the dispersion law, Eq. (3.34): the peaks broaden and become more asymmetric (see the tail on their right side).

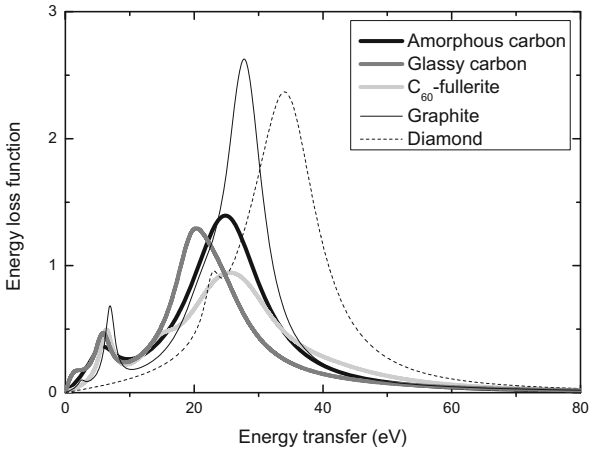

Fig. 3.13 Optical energy loss function of selected allotropic forms of carbon (amorphous carbon, glassy carbon, C60-fullerite, graphite, and diamond) as a function of the excitation energy, calculated by sum of Drude–Lorentz functions, according to Ritchie and Howie [24], using the Garcia-Molina et al. parameters [39]

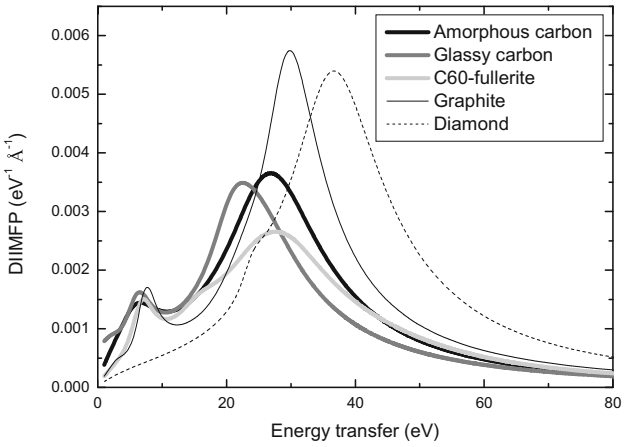

Fig. 3.14 Differential inverse inelastic mean free path for electrons impinging upon several allotropic forms of carbon (amorphous carbon, glassy carbon, C60-fullerite, graphite, and diamond) as a function of the electron energy loss, calculated using Drude–Lorentz functions. The incident electron energy is $E = 250\,\mathrm{eV}$

Figure 3.15 shows, for the five considered allotropic forms of carbon, the electron inelastic mean free path, i.e. the reciprocal of

$$\lambda_{\mathrm{inel}}^{-1} = \int_{W_{\mathrm{min}}}^{W_{\mathrm{max}}} \frac{d\lambda_{\mathrm{inel}}^{-1}}{dw} dw\,, \tag{3.49}$$

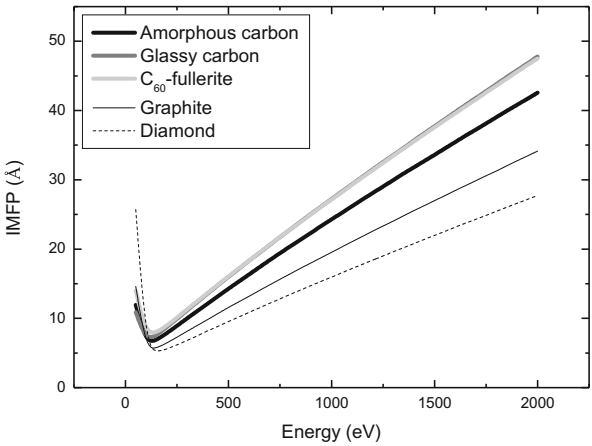

Fig. 3.15 Inelastic mean free path for electrons impinging upon several allotropic forms of carbon (amorphous carbon, glassy carbon, C60-fullerite, graphite, and diamond) as a function of the electron kinetic energy, calculated using Drude–Lorentz functions

where, according to Ref. [38], $W_{\min}$ is set to zero for conductors and to the energy of the band gap for semiconductors and insulating materials. $W_{\max}$ represents the minimum between $E - E_{\text{Pauli}}$ and $(E + W_{\min})/2$. Note that, for metals, $E_{\text{Pauli}} = E_{\text{F}}$. Garcia-Molina et al., recently proposed the value $E_{\text{Pauli}} = 4\,\text{eV}$ for several biomaterials [40]. In the same paper, Garcia-Molina et al. set $W_{\min}$ to the energy gap for the outer-shell electron excitations and to the inner-shell threshold energy for the inner-shell electron excitations [40]. According to Emfietzoglou et al. [38], the factor 1/2 in $W_{\max}$ is due to the fact that electrons cannot be distinguished (with the convention to consider the incident electron as the most energetic one after the collision).

3.3.5 The Mermin Theory

A more accurate approach to the calculation of the ELF is based on the use of the Mermin functions [41] instead of the Drude–Lorentz functions in the sum. This method is the Mermin energy loss function-generalized oscillator strength (MELF-GOS) method proposed by Abril et al. [42]. Details of the MELF-GOS method can be found in Chap. 15. According to Abril et al. [42], a linear combination of Mermin-type energy loss functions, one per oscillator, allows to calculate the electron ELF for any given material. The procedure is very similar to the previous one. Unlike that, Mermin functions are used instead of Drude–Lorenz functions. Please note that the Mermin theory includes the dispersion law, and it is not necessary, as is the case for the Drude–Lorentz approach, to introduce an approximate expression of it to extend the ELF beyond the optical domain. The Mermin differential inverse inelastic mean free path of electrons in PMMA is represented in Fig. 3.16, for kinetic energies of the incident electrons ranging from 50 to 1000 eV.

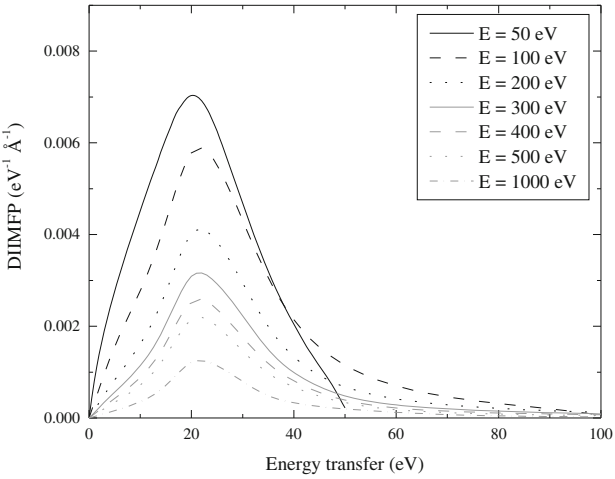

Fig. 3.16 Mermin differential inverse inelastic mean free path of electrons in PMMA as a function of the energy loss for selected values of the incident electron kinetic energy E in the range 50–1000 eV [46]. The calculations are based on the MELF-GOS method [42] (see Chap. 15 for details)

The inverse of the integral of every curve presented in Fig. 3.16 provides, for each kinetic energy E, the inelastic mean free path.

According to de la Cruz and Yubero [43], the values of the inelastic mean free path calculated using the Tanuma, Powell and Penn (TPP) empirical predictive formula [44] are systematically higher than the corresponding values calculated within the Mermin theory. For PMMA, according to our calculation, when $E = 100\,\text{eV}$ the Mermin IMFP is equal to 6.3 Å while when $E = 1000\,\text{eV}$ it is equal to 27.6 Å. According to TPP, the inelastic mean free path of PMMA is equal to 7.9 Å for $E = 100\,\text{eV}$ and to 33.7 Å for $E = 1000\,\text{eV}$ [44]. Approaches based on the Drude–Lorentz theory also provide values of the inelastic mean free path systematically higher than those obtained using the Mermin theory. The inelastic mean free path of PMMA calculated according to the Drude–Lorentz theory is equal to 10.1 Å for $E = 100\,\text{eV}$ and to 33.5 Å for $E = 1000\,\text{eV}$ [45].

3.3.6 *Exchange Effects*

Exchange effects in the electron–electron interaction are due to the fact that scattered electrons cannot be distinguished from ejected electrons. In order to take into account the exchange effects, the differential inverse inelastic mean free path have to be calculated as

$$\frac{d\lambda_{\text{inel}}^{-1}}{d\hbar\omega} = \frac{1}{\pi a_0 E}\int_{k_-}^{k_+}\frac{dk}{k}\left[1 + f_{\text{ex}}(k)\right]\text{Im}\left[\frac{1}{\varepsilon(k,\omega)}\right], \tag{3.50}$$

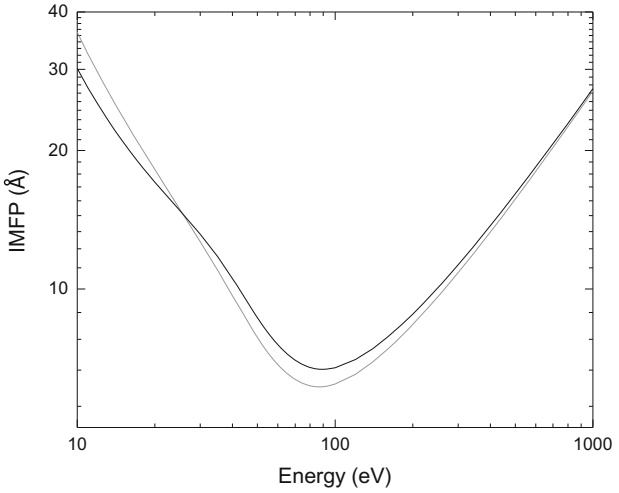

Fig. 3.17 Mermin inelastic mean free path of electrons in PMMA [48] calculated according to the MELF-GOS method [42] (see Chap. 15 for details). *Black line* with exchange. *Gray line* without exchange. *Courtesy* of P. de Vera, I. Abril, R. Garcia-Molina

where, according to the Born–Ochkur approximation [47],

$$f_{\mathrm{ex}}(k) = \left(\frac{\hbar k}{m\upsilon}\right)^4 - \left(\frac{\hbar k}{m\upsilon}\right)^2 . \tag{3.51}$$

In Eq. (3.51) m is the electron mass and υ is the electron velocity.

The Mermin inelastic mean free path of electrons in PMMA, calculated including the Born–Ochkur approximation in order to take into account the exchange effects (black line) is compared, in Fig. 3.17, with the Mermin inelastic mean free path of electrons in PMMA calculated without exchange effects (gray line) [48]. The calculations are based on the MELF-GOS method [42].

3.3.7 Polaronic Effect

A low-energy electron moving in an insulating material induces a polarization field that has a stabilizing effect on the moving electron. This phenomenon can be described as the generation of a quasi-particle called polaron. The polaron has a relevant effective mass and mainly consists of an electron (or a hole created in the valence band) with its polarization cloud around it. According to Ganachaud and Mokrani [7], the polaronic effect can be described assuming that the inverse inelastic mean free path governing the phenomenon – that is proportional to the probability for a low-energy electron to be trapped in the ionic lattice – is given by

$$\lambda_{\text{pol}}^{-1} = C\, e^{-\gamma E} \tag{3.52}$$

where C and γ are constants depending on the dielectric material. Thus the lower the electron energy, the higher the probability for an electron to lose its energy and to create a polaron. This approach implicitly assumes that, once has been generated a polaron, the residual kinetic energy of the electron is negligible. Furthermore, it is assumed that the electron stays trapped in the interaction site. This is quite a rough approximation, as trapped electrons – due to phonon induced processes – can actually hop from one trapping site to another. Anyway, it is often a sufficiently good approximation for Monte Carlo simulation purposes, so that it will be used in this book when we will deal with secondary electron emission from insulating materials.

3.4 Inelastic Mean Free Path

We have already discussed the fact that the main mechanism which determines the inelastic scattering cross-section and the relative energy losses, for energies higher than 50 eV, is the interaction of the incident electrons with the collective excitations of the electron sea, known as plasmons. Such energy loss mechanisms can be described by calculating the so-called energy loss function, i.e., the reciprocal of the imaginary part of the dielectric function. The Ritchie theory [6, 24] can be used – starting from the knowledge of the dependence of the dielectric function upon both the energy loss and the momentum transfer – to calculate the differential inverse electron inelastic mean free path and the electron inelastic mean free path. When the electron energy is higher than 50 eV, both the electron inelastic mean free path and the electron stopping power calculated within the dielectric formalism are in very good agreement with the experiment (and with theoretical data obtained by other investigators).

When, on the other hand, the electron energy becomes lower than 50 eV, the dielectric formalism alone is no longer able to accurately describe the energy loss phenomena. In fact, as the electron energy decreases, the electron inelastic mean free path calculated using only the electron–electron interaction increases indefinitely (see Figs. 3.11 and 3.12), while the stopping power goes quickly to zero (see Figs. 3.9 and 3.10). This means that if only electron–electron interactions were active for inelastic scattering, electrons with such a low energy would no longer interact inelastically (i.e., losing energy) with the solid. As a consequence they would travel without any change in their kinetic energy. For a semi-infinite target, this very long travel in the solid would either continue forever or until the electron reaches the surface of the material and is able to emerge.

As a matter of fact, we know that when the energy becomes lower than 20–30 eV further mechanisms of energy loss becomes very important (electron–phonon and electron–polaron interactions) so that the actual inelastic mean free path approaches zero as the electron energy goes to zero.

3.5 Surface Phenomena

Bulk and surface plasmon losses. The plasma frequency ω_p is given, in the Drude free electron theory, by Eq. (3.30) and represents the frequency of the volume collective excitations, which correspond to the propagation in the solid of *bulk plasmons* with energy

$$E_p = \hbar\omega_p \,. \tag{3.53}$$

In the electron energy loss spectra, it is thus expected to observe a bulk plasmon peak whose maximum is located at an energy E_p [given by Eq. (3.53)] from the elastic or zero-loss peak.

Also, features related to *surface plasmon* excitations appear in spectra acquired either in reflection mode from bulk targets or in transmission mode from very thin samples or small particles [49]. Indeed, in the proximity of the surface, due to the Maxwell's equation boundary conditions, surface excitations modes (surface plasmons) take place with a resonance frequency slightly lower than the bulk resonance frequency.

A rough evaluation of the energy of the surface plasmons can be performed – for a free electron metal – through the following very simple considerations [9]. In general, similarly to the volume plasmons propagating inside the solid, in the presence of an interface between two different materials – which we indicate here with a and b –, longitudinal waves travel as well along the interface. From continuity considerations it follows that [9]

$$\varepsilon_a + \varepsilon_b = 0 \,, \tag{3.54}$$

where we have indicated with ε_a the dielectric function on side a and with ε_b the dielectric function on side b of the interface. Let us now consider the particular case of a vacuum/metal interface and ignore, for the sake of simplicity, the damping, so that $\Gamma \approx 0$. Then, if a represents the vacuum, we have

$$\varepsilon_a = 1 \,, \tag{3.55}$$

and

$$\varepsilon_b \approx 1 - \frac{\omega_p^2}{\omega_s^2} \,, \tag{3.56}$$

where we have indicated with ω_s the frequency of the longitudinal waves of charge density traveling along the surface. Then we obtain, from Eq. (3.54)

$$2 - \frac{\omega_p^2}{\omega_s^2} = 0.$$

As a consequence, the surface plasmon energy $E_s = \hbar\omega_s$, i.e. the surface plasmon peak position in the energy loss spectrum, is expected to be found at an energy

$$E_s = \frac{E_p}{\sqrt{2}} \tag{3.57}$$

from the position of the elastic peak.

Chen and Kwei theory. Chen and Kwei [50] used the dielectric theory to show that the differential inverse inelastic mean free path for electrons emerging from a solid surface can be split up into two terms. The first one is the differential inverse inelastic mean free path in an infinite medium. The second one is the so-called surface term which is related to a surface layer extending on both sides of the vacuum-solid interface. As a consequence, electrons can interact inelastically with the solid even if outside, if they are close enough to the surface. Spectra of electrons originating near to the surface are therefore influenced by these surface effects.

The original version of the Chen and Kwei theory concerned only outgoing projectiles [50]. It was generalized by Li et al. [51] for incoming projectiles. See Chap. 14 for details.

So the theory predicts different trends for the inverse inelastic mean free path (IIMFP) for incoming and outgoing electrons when electrons are close to the surface: in particular, the inverse inelastic mean free path of the incoming electrons is found to slightly oscillate around the mean value, i.e., the bulk inverse inelastic mean free path. This phenomenon is attributed to the behavior of the electrons passing through the surface.

Using the Chen and Kwei theory, one can calculate the dependence on z of the inverse inelastic mean free path, for any given electron kinetic energy. In Figs. 3.18

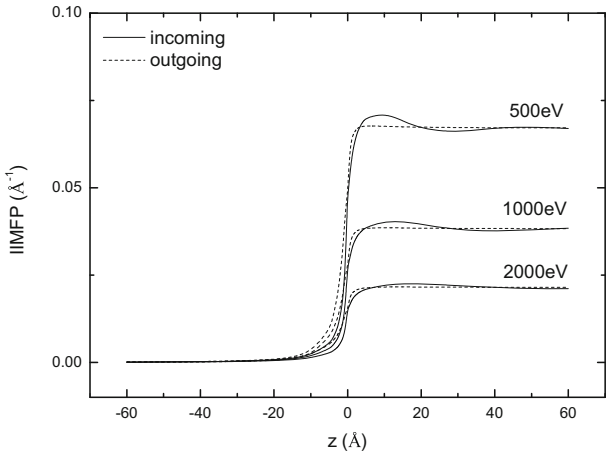

Fig. 3.18 Inverse inelastic mean free path (IIMFP) electrons in Al as a function of the distance from the surface (in the solid and in the vacuum) for several kinetic energies of both incoming and outgoing electrons

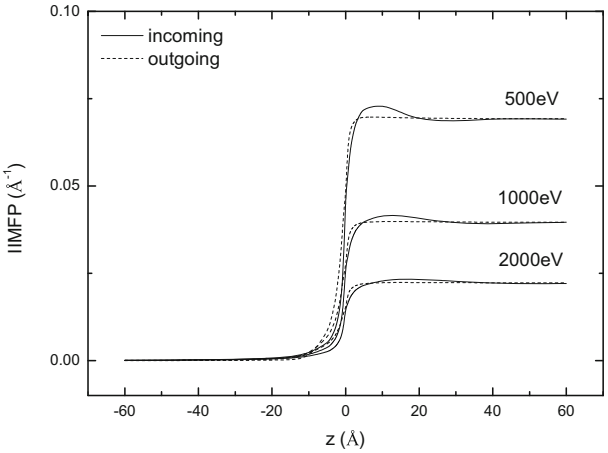

Fig. 3.19 Inverse inelastic mean free path (IIMFP) electrons in Si as a function of the distance from the surface (in the solid and in the vacuum) for several kinetic energies of both incoming and outgoing electrons

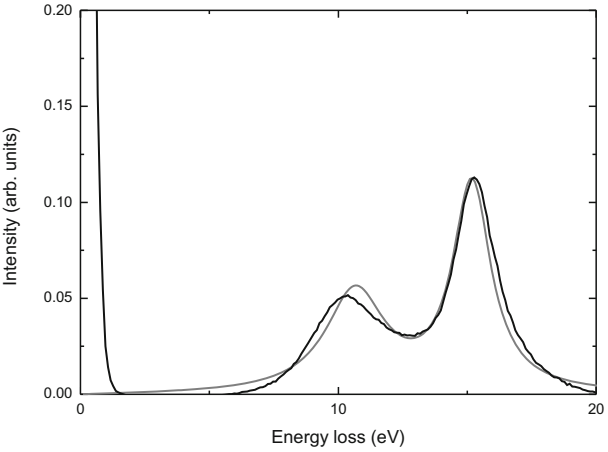

Fig. 3.20 Comparison between the experimental (*black line*) and theoretical (*gray line*) electron energy loss spectra for 1000 eV electrons impinging upon Al [52]. Calculated and experimental spectra were normalized to a common height of the bulk plasmon peak after linear background subtraction. Experimental data: *courtesy* of Lucia Calliari and Massimiliano Filippi

and 3.19 the inverse inelastic mean free path of Al and Si, respectively, are presented as a function of the electron's energy and depth (both outside and inside the solid).

The Chen and Kwei theory [50] and its generalization by Li et al. [51] have been recently used for simulating the surface and bulk plasmon loss peaks in Al and Si [52].

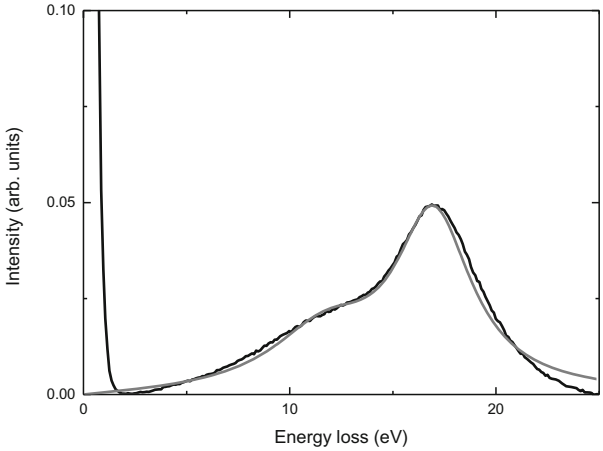

Fig. 3.21 Comparison between the experimental (*black line*) and theoretical (*gray line*) electron energy loss spectra for 1000 eV electrons impinging upon Si [52]. Calculated and experimental spectra were normalized to a common height of the bulk plasmon peak after linear background subtraction. Experimental data: *courtesy* of Lucia Calliari and Massimiliano Filippi

The energy loss spectrum can be calculated under the assumption that experimental spectra arise from electrons undergoing a single large angle elastic scattering event (so-called V-type trajectories [53]). In Figs. 3.20 and 3.21, the present calculation based on the combination of the Chen and Kwei and Li et al. theory [50, 51] with a single V-type trajectory modeling for Al and Si, are compared to experimental data [52]. Calculated and experimental spectra are normalized to a common height of the bulk plasmon peak.

3.6 Summary

In this chapter, elastic and inelastic scattering cross-sections were described. They are the main ingredients of the Monte Carlo simulation.

In particular, the elastic scattering collisions can be calculated by the Mott cross-section, the electron–plasmon inelastic scattering events by the Ritchie dielectric theory, and electron–phonon energy losses by the Fröhlich theory. Polaronic effects can be computed according to Ganachaud and Mokrani.

Chen and Kwei theory and its generalization due to Li et al. were also described. These theories allow to deal with the surface phenomena, particularly important for the investigation of reflection electron energy loss spectroscopy when the incident electron energy is smaller than 2–3 keV.

References

1. N.F. Mott, Proc. R. Soc. Lond. Ser. **124**, 425 (1929)
2. H. Fröhlich, Adv. Phys. **3**, 325 (1954)
3. H.A. Bethe, Ann. Phys. Leipz. **5**, 325 (1930)
4. R.O. Lane, D.J. Zaffarano, Phys. Rev. **94**, 960 (1954)
5. K. Kanaya, S. Okayama, J. Phys. D. Appl. Phys. **5**, 43 (1972)
6. R.H. Ritchie, Phys. Rev. **106**, 874 (1957)
7. J.P. Ganachaud, A. Mokrani, Surf. Sci. **334**, 329 (1995)
8. P. Sigmund, *Particle Penetration and Radiation Effects* (Springer, Berlin, 2006)
9. R.F. Egerton, *Electron Energy-Loss Spectroscopy in the Electron Microscope*, 3rd edn. (Springer, New York, 2011)
10. R.F. Egerton, Rep. Prog. Phys. **72**, 016502 (2009)
11. A. Jablonski, F. Salvat, C.J. Powell, J. Phys. Chem. Data **33**, 409 (2004)
12. M. Dapor, J. Appl. Phys. **79**, 8406 (1996)
13. M. Dapor, *Electron-Beam Interactions with Solids: Application of the Monte Carlo Method to Electron Scattering Problems* (Springer, Berlin, 2003)
14. M.L. Jenkin, M.A. Kirk, *Characterization of Radiation Damage by Electron Microscopy*, IOP Series Microscopy in Materials Science (Institute of Physics, Bristol, 2001)
15. G. Wentzel, Z. Phys. **40**, 590 (1927)
16. S. Taioli, S. Simonucci, L. Calliari, M. Filippi, M. Dapor, Phys. Rev. B **79**, 085432 (2009)
17. S. Taioli, S. Simonucci, M. Dapor, Comput. Sci. Discov. **2**, 015002 (2009)
18. S. Taioli, S. Simonucci, L. Calliari, M. Dapor, Phys. Rep. **493**, 237 (2010)
19. F. Salvat, R. Mayol, Comput. Phys. Commun. **74**, 358 (1993)
20. E. Reichert, Z. Phys. **173**, 392 (1963)
21. M. Dapor, Phys. Rev. B **46**, 618 (1992)
22. J. Llacer, E.L. Garwin, J. Appl. Phys. **40**, 2766 (1969)
23. M.J. Berger, S.M. Seltzer, National Research Council Publication, Whasington D.C. vol. 1133 (1964), p. 205
24. R.H. Ritchie, A. Howie, Philos. Mag. **36**, 463 (1977)
25. F. Yubero, S. Tougaard, Phys. Rev. B **46**, 2486 (1992)
26. H. Raether, *Excitation of Plasmons and Interband Transitions by Electrons* (Springer, Berlin, 1982)
27. A. Cohen-Simonsen, F. Yubero, S. Tougaard, Phys. Rev. B **56**, 1612 (1997)
28. J.J. Ritsko, L.J. Brillson, R.W. Bigelow, T.J. Fabish, J. Chem. Phys. **69**, 3931 (1978)
29. B.L. Henke, P. Lee, T.J. Tanaka, R.L. Shimabukuro, B.K. Fujikawa, At. Data Nucl. Data Tables **27**, 1 (1982)
30. B.L. Henke, P. Lee, T.J. Tanaka, R.L. Shimabukuro, B.K. Fujikawa, At. Data Nucl. Data Tables **54**, 181 (1993)
31. U. Buechner, J. Phys. C: Solid State Phys. **8**, 2781 (1975)
32. D.R. Penn, Phys. Rev. B **35**, 482 (1987)
33. J.C. Ashley, J. Electron Spectrosc. Relat. Phenom. **46**, 199 (1988)
34. J.C. Ashley, J. Electron Spectrosc. Relat. Phenom. **50**, 323 (1990)
35. Z. Tan, Y.Y. Xia, X. Liu, M. Zhao, Microelectron. Eng. **77**, 285 (2005)
36. J.C. Ashley, V.E. Anderson, IEEE Trans. Nucl. Sci. **NS28**, 4132 (1981)
37. S. Tanuma, C.J. Powell, D.R. Penn, Surf. Interface Anal. **17**, 911 (1991)
38. D. Emfietzoglou, I. Kyriakou, R. Garcia-Molina, I. Abril, J. Appl. Phys. **114**, 144907 (2013)
39. R. Garcia-Molina, I. Abril, C.D. Denton, S. Heredia-Avalos, Nucl. Instrum. Methods Phys. Res. B **249**, 6 (2006)
40. R. Garcia-Molina, I. Abril, I. Kyriakou, D. Emfietzoglou, Surf. Interface Anal. (2016). doi:10.1002/sia.5947
41. N.D. Mermin, Phys. Rev. B **1**, 2362 (1970)
42. I. Abril, R. Garcia-Molina, C.D. Denton, F.J. Pérez-Pérez, N.R. Arista, Phys. Rev. A **58**, 357 (1998)

43. W. de la Cruz, F. Yubero, Surf. Interface Anal. **39**, 460 (2007)
44. S. Tanuma, C.J. Powell, D.R. Penn, Surf. Interface Anal. **21**, 165 (1994)
45. M. Dapor, Nucl. Instrum. Methods Phys. Res. B **352**, 190 (2015)
46. M. Dapor, Front. Mater. **2**, 27 (2015)
47. V.I. Ochkur, Sov. Phys. J.E.T.P. **47**, 1766 (1964)
48. P. de Vera, I. Abril, R. Garcia-Molina, J. Appl. Phys. **109**, 094901 (2011)
49. C.J. Powell, J.B. Swann, Phys. Rev. **115**, 869 (1959)
50. Y.F. Chen, C.M. Kwei, Surf. Sci. **364**, 131 (1996)
51. Y.C. Li, Y.H. Tu, C.M. Kwei, C.J. Tung, Surf. Sci. **589**, 67 (2005)
52. M. Dapor, L. Calliari, S. Fanchenko, Surf. Interface Anal. **44**, 1110 (2012)
53. A. Jablonski, C.J. Powell, Surf. Sci. **551**, 106 (2004)